UNIVERSIDADE DE COIMBRA

**Ph.D. Thesis Project**

# Large-Area Time & Position Sensitive RPC for Muography

By

João Pedro Saraiva

**Supervisors**
Ph.D. Alberto Blanco
Ph.D. Isabel Lopes

Coimbra, September 2022

# Abstract

A recent imaging technique using cosmic-ray muons allows to detect the presence of materials with high atomic number inside large volumes. Resistive plate chambers that have been built in Coimbra for years can also be used for this purpose. Preliminary tests were already conducted showing the potential of this technology in the mentioned field. The objective of this Ph.D. thesis is to improve the detector capabilities, bringing it to the front line of the technologies used imaging large-scale object. The present document provides an overview of the subject, the work done during this year and the one to be accomplished in the next two.

# Contents

# List of Figures

# List of Tables

# Acronyms

| | |
|---|---|
| **CTS** | Central Trigger System |
| **DAQ** | Data Acquisition |
| **EMI** | Electromagnetic Interferences |
| **FEE** | Front End Electronics |
| **FWHM** | Full Width at Half Maximum |
| **HV** | High Voltage |
| **MCS** | Multiple Coulomb Scattering |
| **MIP** | Minimum Ionizing Particle |
| **SNR** | Signal-to-Noise Ratio |
| **PCR** | Primary Cosmic-Ray |
| **PoCA** | Point of Closest Approach |
| **RPC** | Resistive Plate Chamber |
| **SCR** | Secondary Cosmic-Ray |
| **SM** | Scattering Muography |
| **TM** | Transmission Muography |

# Introduction

Since there invention in the 1980s, Resistive Plate Chambers (RPCs) have been used in high energy physics experiments and cosmic-ray observatories for fundamental physics research, as well as in a wide range of applications, for instance to measure the cosmic-ray flux from a boat along a meridian until the Antarctica or to image the innards of volcanoes.

Every square centimeter of the surface of Earth at sea level is constantly being hit by approximately one muon per minute. In fact, with an average energy of 4 GeV at sea level, muons are ionizing particles contributing a few percent to the annual background radiation that we are all exposed to. They are created in the atmosphere by Primary Cosmic Rays (PCR) and despite being unstable particles with a mean lifetime of 2.2 µs, most of them reach the ground and even penetrate hundreds of meters below the surface. This highly penetrating capability, combined with the continuous natural flux of muons, make them very suitable to investigate the inside of large objects.

The muography is the method of imaging objects with muons. It is based on the absorption or scattering of muons when passing the target, being subdivided in two branches depending on which of these two physical processes it is related to: the Transmission or absorption Muography (TM) and the Scattering Muography (SM), respectively.

The purpose of this works is to use RPCs to perform SM and develop a novel RPC readout codification allowing to significantly expand the scanned area without increasing the signal readout electronics in the same proportion. The present document provides an overview of the topics that will be covered during the next two years as well as the path to be followed in order to achieve the goal mentioned above. This document contains four chapters. The first one describes the particle source, trying to explain why muons are so unique and important for physics applications. The second chapter explains what muography is about, covering both techniques (TM and SM) and including some applications. The third chapter refers to the detectors used in this project, the RPCs and the preliminary tests performed with them. Finally, the fourth chapter includes a description of the novel readout codification and the methodology to develop and test it. The chapter includes also the plan and objectives for the success of this Ph.D. thesis.

# 1

# Cosmic-Rays

Since the studies of Victor Hess [Hes12], in the early $20^{\text{th}}$ century, it is known that the Earth's atmosphere is constantly being hit by high-energetic particles coming from the outer space. These particles, nowadays known as primary* cosmic-rays (PCRs), are mostly protons (∼90%)†, alpha particles (∼9%) and heavier nuclei with energies from few MeV to hundreds of EeV (tens of Joules) [PDG20, Geo09].

To reach the atmosphere from the vertical of a given geographic location, PCRs must have a minimum energy in order to overcome the geomagnetic field, which is expressed by the vertical cutoff magnetic rigidity. The magnetic rigidity (R) is defined as the particle momentum per unit of charge, as shown in equation 1.1.

$$R = \frac{pc}{Ze} \quad [\text{V}] \tag{1.1}$$

A world map of vertical cutoff rigidities can be seen in figure 1.1. From the figure analysis, for instance a proton with momentum (p) below 1 GeV/c, i.e. with magnetic rigidity below 1 GV, can only cross the geomagnetic field at high latitudes ($> \sim 60°$). On the other hand, a cutoff rigidity above 10 GV is needed for a proton to reach the

*The convention followed in this thesis is to consider "primaries" the cosmic-rays arriving and interacting with the upper layers of the atmosphere, while "secondaries" are the products of such interactions.

†atomic percentages.

atmosphere in the equatorial region.

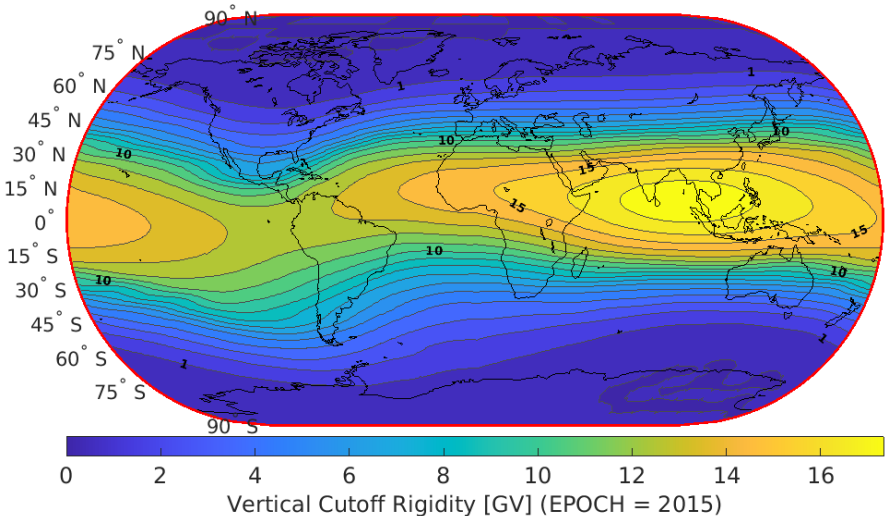


FIGURE 1.1: Vertical cosmic-ray cutoff rigidity [GV] with iso-rigidity contours (adapted from [Sar20] with updated calculations, using the 12$^{\text{th}}$ generation International Geomagnetic Reference Field for epoch 2015, from [Sma21]).

After successfully crossing the magnetic field, PCRs reach the atmosphere, encountering an increasing number of molecules and atoms. The vertical atmospheric thickness ($X$) at a given altitude ($h$) corresponds to the amount of matter penetrated by the particles along their vertical trajectory up to that point and is expressed in units of mass per area. It can be obtained integrating the atmospheric density ($\rho$) along the particle's path (r) as shown in equation 1.2. The relation between atmospheric thickness and altitude above sea level is illustrated in figure 1.2. As can be seen from the figure, the average vertical atmospheric depth at sea level is around 1030 g.cm$^{-2}$.

$$X = \int_{h}^{\infty} \rho \cdot dr \quad [\text{g.cm}^{-2}] \tag{1.2}$$

In the first few hg.cm$^{-2}$, primaries interact with the atmospheric constituents producing an increasing number of secondary cosmic-rays (SCRs) that can reach and be detected at sea level. The particle flux increases with increasing atmospheric depth, with a maximum around 1 hg.cm$^{-2}$, corresponding to an altitude of $\sim$15 km or an atmospheric pressure of 80 mm of mercury as reported by Pfotzer in 1936 (see figure 1.3). At lower distances to sea level, the particle flux decreases continuously while particles lose their energy or decay in the atmosphere.

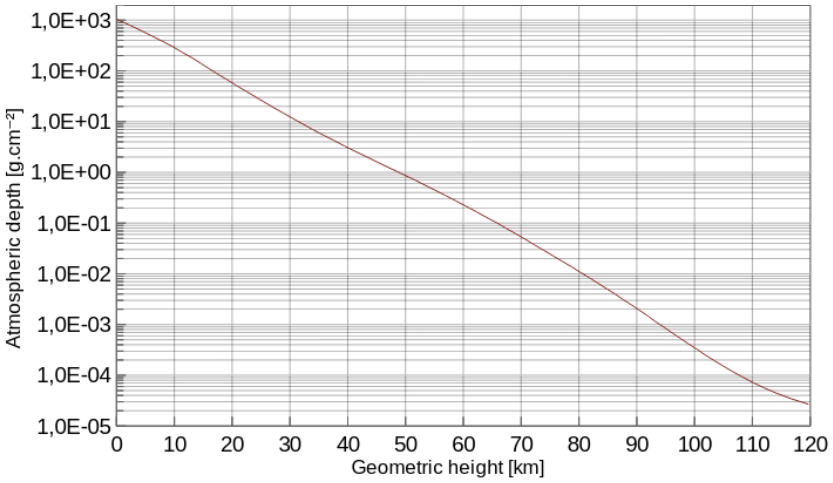


FIGURE 1.2: Vertical atmospheric depth as a function of altitude (0-120km) (data obtained from the COSPAR International Reference Atmosphere; updated version of Barnett and Chandra, 1990) [NAS07]

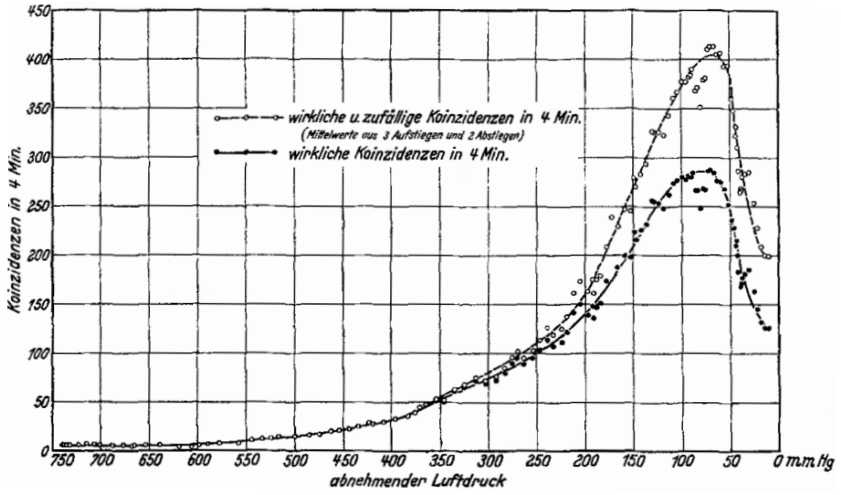


FIGURE 1.3: Particle counting rate of nearly vertical cosmic-rays versus atmospheric pressure, as shown by Pfotzer in 1936: mean values from 3 ascents and 2 descents; real+random coincidences (upper curve), real coincidences (lower curve). [Pfo35, Pfo36]

Upon entering the atmosphere, PCRs mainly interact by ionization and spallation reactions[‡]. While excitation/ionization processes are the most frequent collisions, they play a minor role in the high atmosphere since the energy loss by ionization is relatively

[‡]A list and description of nuclear interactions can be found here [Sar12].

small, 1–2 MeV.cm$^2$.g$^{-1}$ for minimum ionizing particles (MIPs), i.e. only 200 MeV lost by a charged relativistic particle reaching an altitude of 15 km from the vertical direction (∼100 g.cm$^{-2}$). On the other hand, hadronic interactions, i.e. collisions involving the strong interaction[§] between PCRs and atomic nuclei[¶], are much less frequent than Coulomb interactions, however they play a significant role for energy dissipation of primaries with energies in the order of GeV or higher and for production of energetic SCRs. These secondaries in turn collide with further atmospheric nuclei giving rise to the hadronic component of the particle shower (also known as air shower).

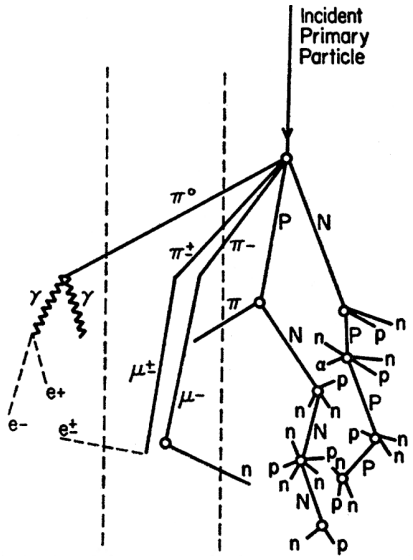


FIGURE 1.4: Schematic representation of the typical development of SCRs within the atmosphere (adapted from [Sim52]).

Three major cosmic-ray components can be distinguished in air showers (see figure 1.4):

1. **Hadronic component:**

   - **light nuclei**: nuclear fragments from the primary impact which may have enough energy to react with further nuclei.
   - **nucleons**: nucleons of high energy (up to the energy of the incident particle and represented by P and N in the figure) ejected from target nuclei in the forward direction, i.e. close to the direction of the parent particles; evaporation

[§] with range in the order of a few femtometers.

[¶] with diameter approximately 5 orders of magnitude lower than the typical electronic clouds.

nucleons (p, n) emitted isotropically from each target nucleus with energies of few MeV.

- **mesons**: charged and neutral pions with production threshold around 290 MeV; mesons of higher mass such as charged and neutral kaons and eta mesons are also produced; all unstable particles that can either decay or interact producing more secondaries; neutral pions and eta mesons decay mainly into two gamma-ray photons, initiating the electromagnetic component of the shower; charged pions decay into muons starting the muonic component of the cascade; kaons also decay producing more pions and muons.

2. **Electromagnetic component:** gamma-ray photons interact with matter mainly via the pair production process while their energy is well above twice the rest mass of the electron, creating electron-positron pairs; these latter particles lose most of their energy by bremsstrahlung emission, i.e. producing more photons; this multiplication process in the electromagnetic shower continues as long as the involved energies are above the electron critical energy[‖], which is about 81 MeV in air.

3. **Muonic component:** the most penetrating part of atmospheric showers[**]; most muons are created around 15 km of altitude (see figure 1.5), where the majority of pions decay ($c\tau$ ~7.8 m)[††]; muons decay into electrons and positrons ($c\tau$ ~660 m) but most of them reach the ground[‡‡] because of time dilation[§§]; the mean energy of muons at sea level is ~4 GeV [PDG20] and in case of vertical trajectory, relativistic muons lose about 2 GeV to reach the ground; below ~1 GeV most of the produced muons decay in the atmosphere (see e.g. the survival probability of muons calculated here [Gri01]).

All particles in air showers interact more or less intensely with the atmospheric constituents. In the case of muons, the main energy loss mechanism when passing through matter is by inelastic scattering with orbital electrons, i.e. via atomic excitations and ionizations. As leptons, muons don't interact via the strong force and having a mass 207 greater than the mass of electrons, their radiative losses are small (Bremsstrahlung losses negligible for energies below few hundred GeV (muon critical energy: $Ec_\mu$ ~1 TeV in

[‖] critical energy (Ec): energy at which ionization and bremsstrahlung loss rates are equal.

[**] neutrinos (chiefly muonic and electronic and the corresponding antiparticles) are also produced by the decay of pions, kaons and muons, however without relevance for this thesis for obvious reasons.

[††] $c\tau$: distance traveled at the speed of light during the particle's mean lifetime.

[‡‡] some muons can even penetrate a few kilometers of rock (see figure 'vertical muon intensity vs. depth' in [PDG20]).

[§§] E.g., a 6 GeV muon has a decay length $\beta\gamma c\tau$ ~38 km, which is of course reduced by energy loss along its trajectory in the atmosphere; for a pion with the same energy: $\beta\gamma c\tau$ ~350 m.

air) [Gri01, PDG20]). Since they are mainly subject to collision losses, muons have very high penetration capabilities compared to other particles and travel large distances in the atmosphere[¶¶].

Muons are the most abundant[***] energetic charged secondaries at sea level since they are the least likely to interact with significant energy loss. In fact from the analysis of figure 1.5 one can see that, for particles above 1 GeV, the vertical flux at sea level consists of almost 100% of muons. The remaining particles are mostly neutrons, protons, electrons and pions.

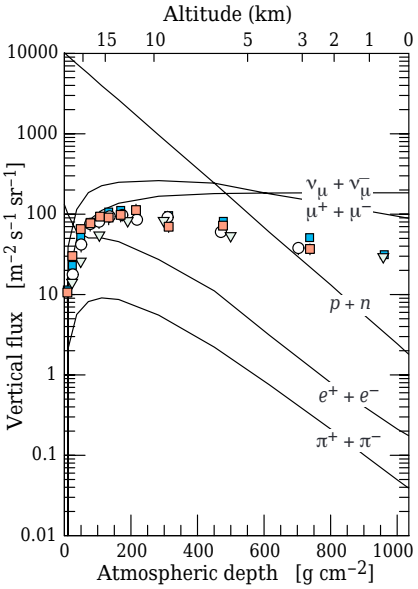


FIGURE 1.5: Calculated vertical fluxes of the major secondary cosmic-ray components with energy above 1 GeV (energy region where the particles are most numerous, except for electrons that are most numerous near their critical energy). The points show measurements of negative muons also with energy higher than 1 GeV. [PDG20]

The overall angular distribution of muons at the ground, as a function of zenith angle ($\theta$), is proportional to $cos^2(\theta)$ [PDG20]. However, this dependence of muon intensity with zenith angle varies with the muon energy as follows: (1) at higher energies ($>\sim$100 GeV), the muon intensity increases with increasing zenith angle[†††]; (2) at lower energies, the

[¶¶]a description of muon energy loss mechanisms (namely: ionization, bremsstrahlung, direct electron pair production, direct muon pair and muon trident production, photonuclear reactions of muons) can be seen here [Gri10].

[***]again, and for the last time, the almost non-interacting neutrinos are not referenced in this work.

[†††]the competition between decay and interaction of pions and kaons of a given energy, created from the first generation of interactions of PCRs, changes in favor of decay with increasing zenith angle since they

effect is opposite because muons decay before reaching the surface[‡‡‡]. As a result, the average muon energy at sea level increases with increasing zenith angle.

The energy spectrum of atmospheric muons at sea level is nearly constant below 1 GeV and falls above 10 GeV reflecting the primary spectrum in the 10–100 GeV range [PDG20]. Above this energy, the muon energy spectrum is steeper than the primary spectrum since pions and kaons of very high energy tend to interact before they decay.

$I_0 = \sim 90\ m^{-2}s^{-1}sr^{-1}$ is the vertical intensity at sea level of muons with momentum above 1 GeV/c, as provided in figure 1.5. Integrating this value over $2\pi$ sr and using the $cos^2(\theta)$ dependency, the result is an overall[§§§] muon intensity (I) at sea level of around 1 $cm^{-2}min^{-1}$ (see equation 1.3) or, equivalently, about 180 muons per square meter and per second.

$$I = \int_\Omega I_0 \cdot cos^2(\theta) = \int_0^{2\pi} d\phi \int_0^{\pi/2} sin(\theta)cos^2(\theta)d\theta = \frac{2}{3}\pi I_0 \quad [\mathrm{Hz.m^{-2}}] \tag{1.3}$$

travel longer in a low density region than when propagating vertically (rate of change of density along an inclined trajectory is smaller per unit path length than along a vertical trajectory [Gri01]). Therefore, for a given pion energy, the likelihood of decay is larger in horizontal direction, enhancing the muon intensity.

[‡‡‡]the angular distribution of low energy muons is proportional to $cos^n(\theta)$ where n is a function of momentum, having an average value of n = 1.85 at 1GeV (see [Gri01] for more details).

[§§§]omnidirectional above the horizon.

# 2
# Muography

As explained in the previous chapter, muons are the most abundant energetic charged SCRs at sea level and have very high penetration capabilities since they are least likely to interact with significant loss of energy. These characteristics qualify muons as the best particles to investigate internal properties of large-scale objects. Two techniques can be used for this purpose. In the first one, the muon counting rate can be measured after passing through a large object. The differential attenuation of muons provides information on the amount of crossed material, allowing for instance to search for cavities on its inside. This method, known as transmission or absorption muography (TM)*, is briefly described below. Another approach, denominated scattering muography (SM), rely on the Coulomb scattering of muons to infer the presence of materials with high atomic number (Z) in large volumes. In this case, the muon tracks must be measured before and after traversing the target, with detectors located in both sides. The SM is the method used along this thesis and is described below in more details.

*The term muography will be used in this work to refer to the imaging techniques based on both: transmission and scattering of atmospheric muons.

## 2.1 Transmission Muography (TM)

With the transmission or absorption-based muography (TM), the detector is located in such a way that it measures the particle flux that went through the large object being studied. I.e., the detector is located on one side of the target, e.g. behind or below it, measuring the natural muon flux during the exposure time required to acquire enough statistics and achieve the intended precision. The passage of muons coming from all directions under the detector acceptance are evaluated and then compared to open sky measurements or Monte Carlo calculations. The muon absorption depends on the density and thickness of the material encountered along their trajectories, or in other words, the particle attenuation is directly related to the opacity of the target along each line of sight. The opacity of the material can be quantified in the same way as performed in the previous chapter with the atmospheric depth: integrating the material density along the muon path length (see equation 1.2). The opacity is generally expressed in g.cm$^{-2}$ or in "meter water equivalent" (mwe)[†]. Measuring the muon attenuation (i.e. the material opacity) and knowing the dimensions of the studied object, its average density can therefore be obtained. The measurements can also be repeated from different orientations in order to produce a 3D representation of the density distribution. The other way around, if an estimation of the density is provided, the boundaries of the object can be extracted.

The dependence of the mean energy loss of muons (and hence their probability of absorption) on the density can be seen directly from the well-known Bethe formula (equation 2.1), bearing in mind that atomic excitation and ionization are the main energy loss processes of most muons used for muography imaging (Ec$_\mu$ ∼500 GeV in standard rock [PDG20]).

$$-\left\langle \frac{dE}{dx} \right\rangle = K\rho\frac{Z}{A}\frac{z^2}{\beta^2}\left[\frac{1}{2}ln\frac{2m_e c^2\beta^2\gamma^2 T_{max}}{I^2} - \beta^2 - \frac{\delta}{2}\right] \quad [\text{MeV.cm}^{-1}] \tag{2.1}$$

The mean stopping-power shown in the equation includes only the correction relevant at high energy regime, which is the density-effect correction. Symbols and values are given in table 2.1.

From the analysis of the Bethe formula, one can see the dependence on the density but also on other parameters intrinsic to the medium crossed by the muons, namely Z, A and the mean excitation energy, I. Nevertheless, in most cases, all the other contributions can be disregarded[‡].

[†] 1 mwe = 100 g.cm$^{-2}$ for $\rho_{H_2O}$=1 g.cm$^{-3}$.

[‡] the Z/A ratio is approximately constant around 0.5 (except for hydrogen), while the contribution of I is reduced by the logarithm factor in the formula.

| Symbol | Definition | Value or Unit |
|---|---|---|
| K | $4\pi N_A r_e^2 m_e c^2$ | 0.3070749 MeV.cm$^2$.mol$^{-1}$ |
| $N_A$ | Avogadro's constant | $6.02214076\times10^{23}$ mol$^{-1}$ |
| $r_e$ | classical electron radius | 2.8179403262(13) fm |
| $m_e c^2$ | electron mass $\times c^2$ | 0.51099895000(15) MeV |
| c | speed of light | 299792458 m.s$^{-1}$ |
| $\rho$ | density | g.cm$^{-3}$ |
| Z | atomic number of absorber | |
| z | charge number of incident particle | |
| A | atomic mass of absorber | g.mol$^{-1}$ |
| $\beta$ | particle speed normalized to c (v/c) | |
| $\gamma$ | Lorentz factor ($1/\sqrt{1-\beta^2}$) | |
| $T_{max}$ | maximum energy transfer in a collision $2m_e c^2\beta^2\gamma^2/(1+2\gamma m_e/M+(m_e/M)^2)$ | MeV |
| I | mean excitation energy of medium (I=f(Z)) | eV |
| $\delta$ | density effect correction* | |

* relevant for high energies: the electric field flattens and extends as the particle energy increases; the field polarizes the medium which in turn limits its extension: electrons far from the particle path are shielded from the full field intensity, reducing the energy loss; $\delta$ depends on the particle speed and on the matter density (higher induced polarization in condensed materials). [Leo94]

TABLE 2.1: Variables used in the Bethe stopping-power formula. [PDG20, BIP19, COD18]

### 2.1.1 Applications of Transmission Muography

TM can be used to study massive bodies such as mountains or volcanoes which may imply data acquisition times of several months. The rationale being for instance to investigate the thickness of rock overlying an underground facility, as performed for the first time by E. George in Australia in 1955. L. Alvarez, in turn, tried to find hidden chambers in the pyramid of Chephren at Giza in 1968, installing two spark chambers of 1.8x1.8 m$^2$[§], separated vertically by a distance of 30 cm and externally triggered by three scintillators located above and below the spark chambers[¶]. After months acquiring events signaled by all three scintillators, no voids were found in the pyramid, however it was possible to clearly identify its four diagonal ridges, as depicted in figure 2.1. Since then, the TM has been employed in numerous applications.

[§]two modules (0.9×1.8 m$^2$) per spark chamber, installed side-by-side.
[¶]with a detector acceptance angle around 35° (half-angle of a vertically oriented cone).

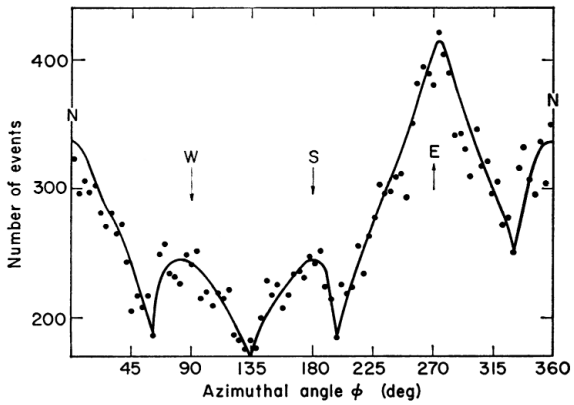


FIGURE 2.1: Variation of the cosmic-ray intensity with azimuthal angle (zenith angle of counts from 20° to 40°) as measured in the "Belzoni chamber" underneath the base of the pyramid of Chephren and near its center. The detector was located 15.5 m east and 4 m north of the center of the pyramid, explaining the difference in the maximum counting rates through the east-west and north-south directions. [Alv70]

The Resistive Plate Chambers (RPCs), described in the next chapter, were also used recently to image several structures, such as the Puy de Dôme volcano in France [Car13, Men16]. At the time of writing this thesis, the Lousal mine in Portugal is also being imaged with RPC detectors; more details can be found here [Afo22, Tei22]. The rapidly growing applications of TM includes for instance borehole muon detectors used to detect geological structures. In case of mid-size targets, for instance nuclear waste containers, the exposure time is significantly lower than the required time in the Alvarez's experiment, since the opacity of the object is much smaller. However, in cases where the rapidity of response is crucial, such as for cargo inspection in the homeland security area, the imaging technique typically employed involves the SM, described in the next section.

## 2.2 Scattering Muography (SM)

### 2.2.1 Multiple Coulomb Scattering (MCS)

The main energy loss process of muons reaching ground is via inelastic scattering with orbital electrons[‖], as briefly mentioned in the previous chapter and described in the section above. This loss mechanism results in a quasicontinuous slowing down of charged particles passing through matter, which is the process upon which the TM is based. The

[‖] also known as (excitation and) ionization losses.

inelastic scattering of muons with nuclei, in turn, results in radiative losses[**] along with their trajectory deflection, however this type of interaction can be neglected if the energy of the particles is well below their critical energy in the material they are passing through. Elastic scattering with nuclei also occurs frequently but less than inelastic collisions with electrons. Through this process, particles suffer deflections in the intense electric field near nuclei but do not radiate. The incident particles lose only the kinetic energy required for conservation of momentum with their target nuclei. Therefore, the latter process has negligible impact on energy loss[††] of particles but dominate their angular deflection in matter, and is the basis for the SM technique. [Eva55, Leo94]

The vast majority of deflections of heavy charged particles traversing a medium are very small as shown by Rutherford, Geiger and Marsden in the early $20^{th}$ century, with the probability of angular deflection of $\alpha$ particles in a thin foil of gold ($\sim 0.2\ \mu m$) being proportional to: (1) the inverse fourth power of the $\sin(\theta/2)$, with $\theta$ the scattering angle of the incident particles, (2) the inverse fourth power of the velocity of the $\alpha$ particles ($v_\alpha$) and (3) the square of the charge (Ze) of the scattering nuclei, as illustrated by equation 2.2. The statistical cumulative effect of many small-angle scatterings, suffered by charged particles when traversing a material, is a deflection from their original direction, whose angular distribution roughly follows a normal distribution with non-Gaussian tails due to the rare large-scattering events. The shape and characteristic width of the Multiple Coulomb Scattering (MCS) distribution can be described by the Molière's theory, however simple approximations exist for practical reasons. [Gei13, PDG20]

$$\frac{d\sigma}{d\Omega} \propto \frac{Z^2}{v_\alpha^4 sin^4(\theta/2)} \tag{2.2}$$

The Lynch & Dahl formula (equation 2.3) is frequently used as proxy for the Molière's theory and provides the rms width of a Gaussian approximation of the central 98% of the MCS angular distribution projected onto a plane containing the initial trajectory. The formula is based on a previous one, the Highland's formula, which, in turn, was established by fitting the Bethe variant[‡‡] of the Molière's theory [Got93]. Lynch & Dahl improved the constants of the Highland's formula by using maximum likelihood fits to 98% of the central part of projected angular distributions generated by Monte Carlo code[§§] [Lyn91].

[**] which includes the bremsstrahlung emission, direct electron pair production, photonuclear reactions and rarer interactions.

[††] except for low-energy heavy particles that can lead to atomic displacements (non-ionizing energy losses (NIEL)).

[‡‡] using Z(Z+1) instead of $Z^2$ to take into account the scattering induced by atomic electrons.

[§§] $10^6$ scatters of singly charged heavy particles simulated for materials of different atomic numbers (Z) and thicknesses.

| Symbol | Definition |
|---|---|
| p | momentum of the incident particle [MeV/c] |
| $\beta$c | velocity of the incident particle (in units of c) |
| z | charge number of the incident particle |
| x/$X_0$ | thickness of the scattering medium in radiation lengths |
| $\theta_0$ | rms width of the projected distribution (rad) |
| $\theta_{space}$ | deflection angle (nonprojected) (sr) |
| $\theta_{plane,x}; \theta_{plane,y}$ | orthogonal projections of the deflection angle* (rad) |

* the orthogonal projections on x and y planes are independent and identically distributed.

TABLE 2.2: Symbols in the Lynch & Dahl formula and related distributions using the same notation as in [PDG20].

Their formula was later compared, for instance, to the MCS of 160 MeV protons in several materials, showing to be in good agreement with the experimental data [Got93]. However, for large Z materials and small thicknesses, it might significantly overestimate the Molière scattering angle [Lyn91, PDG20].

$$\theta_0 = \frac{13.6 \text{ MeV}}{\beta cp} z \sqrt{\frac{x}{X_0}} \left[1 + 0.038 ln\left(\frac{xz^2}{X_0 \beta^2}\right)\right] \quad \text{rad} \tag{2.3}$$

Symbol definitions are given in table 2.2.

The respective projected angular distribution, with zero mean deflection, is given by

$$\frac{1}{\sqrt{2\pi}\theta_0} e^{-\frac{1}{2}\left(\frac{\theta_{plane}}{\theta_0}\right)^2} d\theta_{plane}, \tag{2.4}$$

and the corresponding nonprojected angular distribution:

$$\frac{1}{2\pi\theta_0^2} e^{-\frac{1}{2}\left(\frac{\theta_{space}}{\theta_0}\right)^2} d\Omega, \tag{2.5}$$

where $\theta^2_{space} \approx \theta^2_{plane,x} + \theta^2_{plane,y}$ and $d\Omega \approx d\theta_{plane,x}\, d\theta_{plane,y}$. [PDG20]

The scattering medium dependence of equation 2.3 is entirely provided by the radiation length ($X_0$). Although MCS is not a radiative phenomenon, $\theta_0$ depends on the material's atomic number (Z) and weight (A) in a similar way as given by $X_0$ [Ros41]. This explains why the Lynch & Dahl formula and the ones that preceded it use the material thickness measured in radiation lengths. In order to compute the rms scattering angle of muons in different targets, one might use tabulated values of radiation length for each material, e.g. from [Tsa74] or perform a quick estimate using equation 2.6 provided here [Leo94].

| Material | Z | $X_0$ [cm] | $\theta_0$ (mrad) | $\theta_0$ (deg) |
|---|---|---|---|---|
| Al | 13 | 8.99 | 3.60 | 0.21 |
| Fe | 26 | 1.80 | 8.55 | 0.49 |
| Ag | 47 | 0.87 | 12.57 | 0.72 |
| W | 74 | 0.35 | 20.46 | 1.17 |
| U | 92 | 0.31 | 21.96 | 1.26 |

TABLE 2.3: Rms scattering angles of 4 GeV muons crossing 10 cm thick layers of different materials.

$$X_0 = \frac{716.4\,A}{Z(Z+1)ln(287/\sqrt{Z})} \quad [\text{g.cm}^{-2}] \tag{2.6}$$

Table 2.3 shows rms scattering angles of 4 GeV muons, computed with equations 2.3 and 2.6 for several targets.

While the angular deflection of muons traversing a material is the physical property of interest measured by SM, it can be seen as a side effect for the TM. On the other hand, TM rely on muon absorption in large targets, which corresponds to a loss of signal in the case of SM. In fact, since the width of the MCS distribution increases with the material atomic number, it is possible to distinguish between high and low-Z materials measuring muon trajectories upstream and downstream a probed volume. Several reconstruction techniques might be used to identify the location of higher deflections in a 3D region; the Point of Closest Approach (PoCA) is one of them and is described in the next section.

### 2.2.2 Point of Closest Approach (PoCA) Algorithm

As previously mentioned, in order to differentiate between high and low-Z materials, muon trajectories must be known before and after impinging the object being studied. This can be done, measuring at least four points of each muon path, two upstream and two downstream the target, as shown in figure 2.2. Of course, a large number of events is needed to identify the presence of large-Z materials using the SM technique, just like with the TM to perform average density maps.

The Point of Closest Approach (PoCA) algorithm can be used to identify the location of high scattering events and in this way, reconstruct a 3D image of the respective object. The PoCA algorithm relies on two basic premises: (1) the muon suffers a single Coulomb scatter in the target instead of multiple scatterings and (2) the location of the scattering point coincides with the point of closest approach between the incident and exiting trajectories (the PoCA point). Being a stochastic process, and using a large number of trajectories,

the algorithm allows the 3D reconstruction of a high-Z material, with each PoCA point corresponding to a point in the target. In the case of coplanar incoming and outgoing trajectories, the PoCA point is simply their intersection, otherwise it corresponds to the midpoint of the shortest distance between the two trajectories, as depicted in figure 2.3.

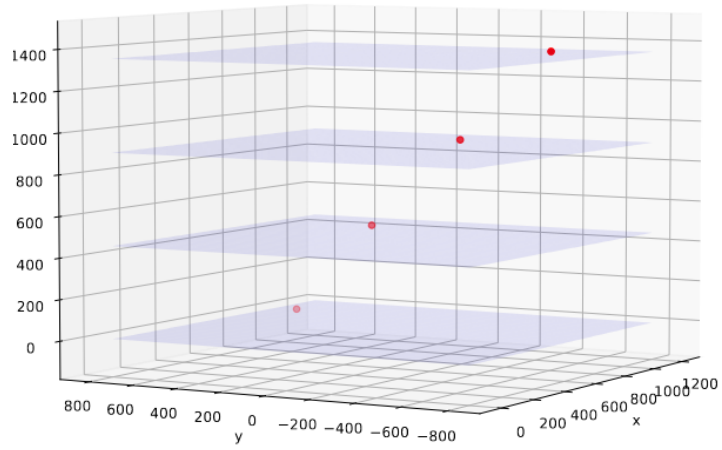


FIGURE 2.2: Four points of a muon track, each measured by a resistive plate chamber with 1.6×1.2 $m^2$ of active area (represented by blue horizontal planes); a target of Tungsten (Z=74) is located between the inner detectors (not represented in the figure); the points in the two upper planes define the incoming trajectory (upstream the target), while the points in the lower planes define the outgoing one (downstream the target).

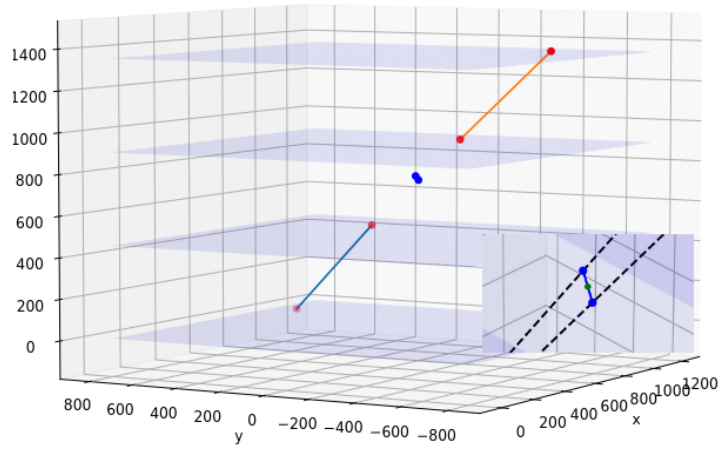


FIGURE 2.3: Same muon path as in figure 2.2; the blue points represent the intersections between extrapolated tracks (incoming and outgoing) and their common perpendicular; the PoCA point (midpoint of the common perpendicular between the intersection points) is shown in the lower right corner of the figure (green point).

rectangular readout electrodes (pads) made of copper and located only on the top of the plastic box, however readout strips are also used frequently. The last layer consists of an aluminum box that surrounds the whole RPC, reducing in this way electromagnetic interferences (EMI) and increasing at the same time the detector robustness and making it easy to transport.

The number of gaps in an RPC might differ from the ones showed in figure 3.1, however its principle of operation is similar and can be described in simple terms as follows: the gaps are filled with a proper gas mixture and an adequate voltage difference is applied between the anode (+HV) and the cathode (-HV) in such a way that when a ionizing particle impinges the gas, it creates ion-electron clusters[¶] along its path. The ions and electrons start drifting to the corresponding electrode due to the presence of the strong electric field. During their path towards the anode, the electrons can create additional ion-electron pairs starting an avalanche of ionizations. The movement of the avalanches in the gas gaps, in turn, induce current pulses in the closest signal readout electrodes that can be, frequently after a previous front-end amplification, exploited by the Data Acquisition (DAQ) system. The signal induction on readout electrodes, i.e. on the outermost layer of the RPC, only occurs because the inner layers (glass[‖] and graphite paint), are transparent to rapid signals, thanks to their high resistivity [Abb18]. A detailed description of the creation of the avalanche, its development and the related physical effects, as well as the development of the induced signal will be provided in the final document of this thesis.

The gas mixture must be chosen in such a way that the avalanches remain confined close to the path of the primary particle and does not extend to the whole gas volume. An hydrofluorocarbon gas such as the R-134a (1,1,1,2-tetrafluoroethane) is frequently chosen together with small proportions of other gases, such as the $SF_6$ (sulphur hexafluoride). With almost four times the air density and high electronegativity, the R-134a can create a high density of clusters, while reducing the amount of free electrons in the gas and in this way the transversal propagation of the avalanches. The $SF_6$, with even higher density and strong electronegativity helps to limit the streamer probability. The addition of a gas with quenching properties, i.e. with high ultraviolet-absorption coefficient, such as the isobutane (methylpropane), contributes also to keep the avalanche well localized in space, avoiding the creation of photoelectrons. [Abb18]

## 3.2 Scattering Muography Test

As explained in section 2.2.2, the SM requires the measurement of at least four points of each muon trajectory, two on either target side. After having four intersection points between the muon trajectories and the RPC planes, the following quantities are computed: (1) the direction of the incoming and outgoing muon paths; (2) the angular deflection suffered by each muon; (3) the PoCA point for each event. Since the PoCA algorithm operates on the assumption that the PoCA points

[¶]Clusters include the primary ion-electron pairs directly generated by the ionizing particle plus additional pairs created by the expelled electrons in case their kinetic energy is high enough for further ionizations ($\delta$ rays). The vast majority of clusters along MIP tracks does not exceed one or few ion-electron pairs, with only $\sim 0.1\%$ having more than 10 pairs in the investigated gases [Fis91].

[‖]or other resistive electrode.

correspond to single Coulomb scattering events occurred in the object, its 3D reconstruction can be achieved by plotting all the PoCA points complying with a certain angular restriction.

Preliminary tests of SM were performed for the first time in Coimbra in 2021 with four horizontally oriented RPCs spaced by 45 cm, each with an active area of 1.6×1.2 $m^2$ and operated in open gas loop with R134a, only. Figure 3.2 provides additional details of the RPCs, including a picture showing several targets being imaged by the four-plane telescope. The RPC specifications can be seen in table 3.1.

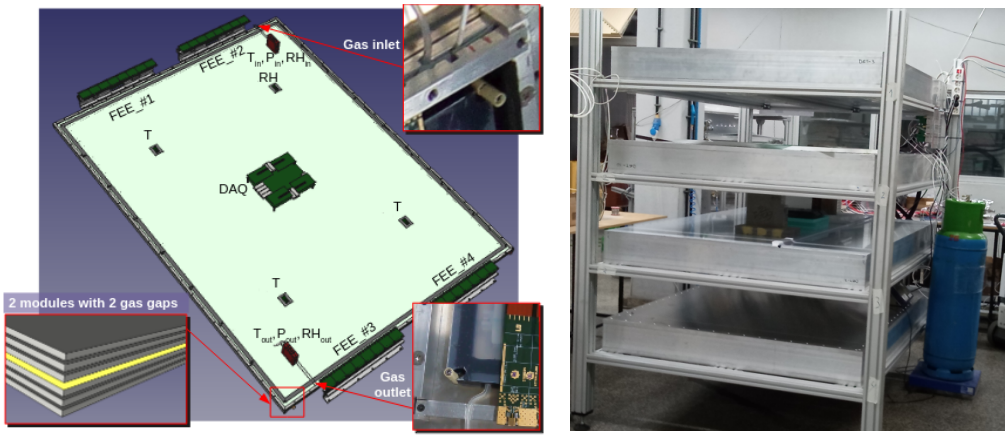


(a) (b)

FIGURE 3.2: (a) 3D view of an RPC with the Front End Electronics (FEE) at both ends, the DAQ at the center and showing also the location of several environmental sensors (temperature (T), atmospheric pressure (P) and relative humidity (RH)); top-right: gas inlet; bottom-right: gas outlet; bottom-left: two sensitive volumes, with two gas gaps 1 mm wide and glass 2 mm thick, separated by the readout strips (not shown for better understanding but with their location represented in yellow) (adapted from [Sar22]) (b) Telescope comprised of four RPCs with targets being imaged at the center.

The signal induced by muons crossing the detector planes are collected by 64 longitudinal readout strips, 1.55 cm wide and with a 1.85 cm pitch (see figure 3.3). The analog pulses are then fed to pre-amplifiers located at both sides of each RPC, as depicted in figure 3.2. In case of pulses with amplitude above a certain threshold, their arrival time and integrated charge are encoded, respectively, by the rising edge and width of a digital signal created by the FEE[**] and sent to the DAQ. If a particle is seen[††] by a majority of 3 out of 4 RPCs, the Central Trigger System (CTS) requests the event recording. Each strip provides 2 values of time ($T_F$ from the front side and $T_B$ from the back side of the RPC) and 2 values of charge ($Q_F$ and $Q_B$). The average front and back values: $(T_F+T_B)/2$ and $(Q_F+Q_B)/2$, correspond to the time and charge of the induced signal in each strip, respectively. Moreover, to determine the 2D position of the particle in each RPC, the

[**]additional information about the charge to width algorithm used by the FEE can be seen here [Bel10].

[††]to infer that the particle was detected, the implemented logic in the DAQ requires having, at the same time, a pulse at both sides of at least one strip of the RPC.

following approach is used: the strip of highest charge value provides the position in one dimension (X), while $(T_F\text{-}T_B)/2$ gives the position in the other direction (Y) (along the strip).

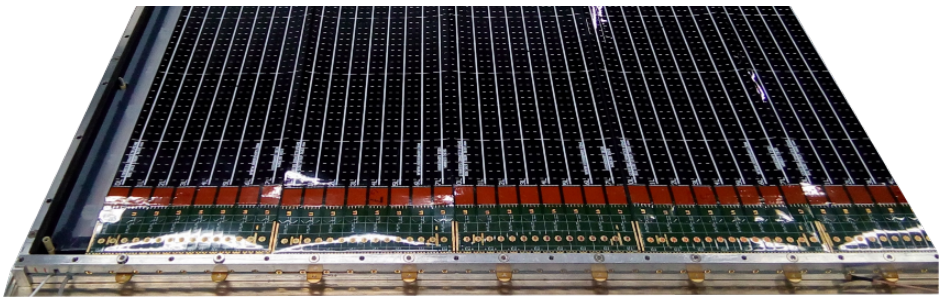

FIGURE 3.3: Detailed view of the pickup strips.

The poor angular resolution achieved during this preliminary test (see table 3.1) is in part due to the short distance between RPC planes, positioned only $\sim$ 22 cm to the object being imaged. To detect scattering angles around 1°, corresponding to the rms deflection produced by 10 cm of tungsten (see table 2.3), RPCs with similar spatial resolution should have been placed 10 times further away. This result explains why the best image of the tungsten target shown in figure 2.4, was obtained selecting only PoCA points with deflections above $\sim$ 11°. Such a high angular restriction allowed to maximize the Signal-to-Noise Ratio (SNR), as clearly observed experimentally, however at the price of discarding a significant amount of good events. The other approach would be, of course, to improve the position resolution of each detector, which can be achieved for instance increasing the number of readout electrodes. Nevertheless, this would have a clear impact on the cost per unit of covered area, mainly because of the additional electronic channels required. One can also try to implement a system increasing the readout strips while keeping unchanged the number of electronic channels. This innovative readout codification is the main goal of this Ph.D. thesis, as explained in the next chapter.

| | |
|---|---|
| Time resolution | 350 ps |
| Spatial resolution | x: 8.5 mm ($\sigma$), y: 1.6 cm ($\sigma$) |
| Angular resolution* | $\theta_x$: 5.1° (FWHM), $\theta_y$: 9.5° (FWHM) |
| Angular acceptance | x: 42°, y: 50° |
| Efficiency** | 99% |

* $\tan^{-1}(\text{FWHM}/(\text{L}/2))$; L: distance between inner RPCs.
** with a Reduced electric field of 235 Td.

TABLE 3.1: Four-plane telescope specifications.

# Conclusion and Final Remarks

Cosmic-ray muons have been used for decades to study the inside of massive objects, such as mountains and volcanoes. The natural flux of muons at sea level along with their unique properties make them the most suitable particle to image such large-scale objects. On the other hand, gaseous detectors such as RPCs are a good choice to cover wide areas at moderate cost. The technique of imaging a target using muons, called along this document as muography, can be divided in two modalities depending on which energy loss mechanism it is related to. While the transmission muography is based on inelastic scattering with orbital electrons and measures the muon attenuation after passing through a target volume, the scattering muography in turn rely on elastic scattering with nuclei, measuring the angular deflection of muons in large-Z materials. The latter method has only been introduced in the present century.

The main objectives of this Ph.D. thesis can be summarized as follows: (1) investigate an optimized RPC configuration in order to perform large-scale scattering muography, maximizing the target detection in the shortest possible exposure time; (2) develop a novel RPC readout codification allowing to keep the number of readout channels as low as possible despite the increase of the detector area. This novel readout codification is expected to be the main research contribution of the thesis. Knowing that a significant share of the detector cost is electronics related, this new readout could potentially position RPCs as the best detector option in fields such as homeland security and border control.

# References


[Abb18] M. Abbrescia, V. Peskov, and P. Fonte. *Resistive Gaseous Detectors*. Wiley-VCH, 2018. ISBN 978-3-527-34076-7. 20, 21

[Afo22] L. Afonso, I. Alexandre, S. Andringa, et al. *Muography in the university and in the museum. Journal of Advanced Instrumentation in Science*, (278), 2022. doi:10.31526/JAIS.2022.278. 12

[Alv70] L. Alvarez, J. Anderson, F. E. Bedwei, et al. *Search for hidden chambers in the pyramids. Science*, 167, 1970. iv, 12

[Bel10] D. Belver, P. Cabanelas, E. Castro, et al. *Performance of the low-jitter high-gain/bandwidth front-end electronics of the hades trpc wall. IEEE Transactions on Nuclear Science*, 57(5):2848–2856, 2010. doi:10.1109/TNS.2010.2056928. 22

[BIP19] BIPM. *The International System of Units (SI)*. BIPM - International Bureau of Weights and Measures, 2019. ISBN 978-92-822-2272-0. 11

[Bla15] A. Blanco, J. Adamczewski-Musch, K. Boretzky, et al. *Performance of timing resistive plate chambers with relativistic neutrons from 300 to 1500 MeV. Journal of Instrumentation*, 10(02):C02034–C02034, 2015. doi:10.1088/1748-0221/10/02/c02034. 20

[Bor03] K. N. Borozdin, G. E. Hogan, C. Morris, et al. *Radiographic imaging with cosmic-ray muons. Nature*, 422:277, 2003. 18

[Car13] C. Carloganu, V. Niess, S. Béné, et al. *Towards a muon radiography of the puy de dôme. Geoscientific Instrumentation Methods and Data Systems*, 2(1):55–60, 2013. doi:10.5194/gi-2-55-2013. 12, 19

[COD18] CODATA - Committee on Data for Science and Technology. *CODATA recommended values of the fundamental physical constants*. `https://www.nist.gov/`, 2018. 11

[Eva55] R. Evans. *The Atomic Nucleus*. McGraw-Hill, 1955. 13

[Fis91] H. Fischle, J. Heintze, and B. Schmidt. *Experimental determination of ionization cluster size distributions in counting gases. Nuclear Instruments and Methods in Physics Research A*, 301:202–214, 1991. 21

[Gei13] H. Geiger and E. Marsden. *The laws of deflexion of $\alpha$ particles through large angles. Philosophical Magazine*, 25(604), 1913. 13

[Geo09] J. S. George, K. A. Lave, M. E. Wiedenbeck, et al. *Elemental composition and energy spectra of galactic cosmic rays during solar cycle 23. The Astrophysical Journal*, 698(2):1666–1681, 2009. doi:10.1088/0004-637x/698/2/1666. 2

[Got93] B. Gottschalk, A. Koehler, R. Schneider, et al. *Multiple Coulomb scattering of 160 MeV protons. Nuclear Instruments and Methods in Physics Research B*, 74:467–490, 1993. 13, 14

[Gri01] P. Grieder. *Cosmic Rays at Earth*. Elsevier, 2001. 6, 7, 8

[Gri10] P. Grieder. *Extensive Air Showers*. Springer, 2010. 7

[Hes12] V. Hess. *Über beobachtungen der durchdringenden strahlung bei sieben freiballonfahrten. Physikalische Zeitschrift*, 13:1084–1091, 1912. 2

[Leo94] W. Leo. *Techniques for Nuclear and Particle Physics Experiments*. Springer-Verlag, 1994. 11, 13, 14

[Lyn91] G. R. Lynch and O. I. Dahl. *Approximations to multiple Coulomb scattering. Nuclear Instruments and Methods in Physics Research B*, 58:6–10, 1991. 13, 14

[Men16] E. L. Menedeu. *RPC application in muography and specific developments. Journal of Instrumentation*, 11(06):C06009–C06009, 2016. doi:10.1088/1748-0221/11/06/c06009. 12

[NAS07] NASA National Space Science Data Center (2007). *Cospar international reference atmosphere (CIRA-86)*, 2007. iv, 4

[PDG20] PDG. *Prog. Theor. Exp. Phys. 2020, 083C01*, 2020. iv, 2, 6, 7, 8, 10, 11, 13, 14

[Pfo35] G. Pfotzer and E. Regener. *Vertical intensity of cosmic rays by threefold coincidences in the stratosphere. Nature*, 1935. iv, 4

[Pfo36] G. Pfotzer. *Dreifachkoinzidenzen der ultrastrahlung aus vertikaler richtung in der stratosphäre. Zeitschrift für Physik*, 1936. iv, 4

[Ros41] B. Rossi and K. Greisen. *Cosmic-ray theory. Reviews of Modern Physics*, 13:240–309, 1941. 14

[San81] R. Santonico and R. Cardarelli. *Development of resistive plate counters. Nuclear Instruments and Methods in Physics Research*, 187(2–3):377–380, 1981. 19

[Sar12] J. P. Saraiva. *Radiological characterization of TFA metallic tubes from CERN accelerator complex*. Master's thesis, Coimbra University, 2012. 4

[Sar20] J. P. Saraiva, A. Blanco, J. Garzón, et al. *The TRISTAN detector—2018–2019 latitude survey of cosmic rays. Journal of Instrumentation*, 15(09):C09024–C09024, 2020. doi:10.1088/1748-0221/15/09/c09024. iv, v, 3, 20

[Sar22] J. Saraiva, C. Alemparte, D. Belver, et al. *Advances towards a large-area, ultra-low-gas-consumption RPC detector. Nuclear Inst. and Methods in Physics Research, A (Under Review)*, 2022. v, 22

[Sim52] J. A. Simpson, W. Fonger, and S. B. Treiman. *Cosmic radiation intensity-time variations and their origin. Physical Review*, 90(5), 1952. iv, 5

[Sma21] D. F. Smart and M. A. Shea. *Vertical geomagnetic cutoff rigidities for epoch 2015*. In *Proc. of the 36th International Cosmic Ray Conference*, ICRC, 2021. doi:10.22323/1.358.1154. iv, 3

[Tei22] P. Teixeira, L. Afonso, S. Andringa, et al. *Muography for underground geological surveys: Ongoing application at the lousal mine. Journal of Advanced Instrumentation in Science*, (278), 2022. doi:10.31526/JAIS.2022.287. 12

[Tsa74] Y.-S. Tsai. *Pair production and bremsstrahlung of charged leptons. Reviews of Modern Physics*, 46(4):815–851, 1974. 14